Thermal Analysis of an Oil-Cooled Shaft for a 30,000 rpm Automotive Traction Motor

Yaohui Gai[1], Yew Chuan Chong[1], Husain Adam[1], Xu Deng[2], Mircea Popescu[1] and James Goss[1]

[1] Motor Design Ltd., Wrexham, LL13 7YT, U.K.

[2] Newcastle University, Newcastle upon Tyne, NE1 7RU, U.K.

.

Abstract—**This paper investigates an oil-based shaft cooling system as applied to a 30,000 rpm automotive traction motor. Firstly, iron and air friction losses are identified over a range of operating speeds. Analytical and numerical approaches are then proposed to estimate thermal performance of steady and dynamic states, respectively. Finally, experiments are conducted to evaluate the impact characteristics of this cooling system, such as the rotational speed, the inlet coolant velocity and the amount of heat loss. Based on simulation and testing of prototype, the shaft rotational velocity can significantly enhance the heat exchange between coolant and internal surface of the hollow-shaft, across whole length of the shaft. However, when the rotational velocity reaches 30,000 rpm, the effect of high rotational velocities on heat exchange weakens due to the flow becoming saturated.**

Index Terms—**Oil cooling, thermal analysis, traction motors, hollow-shaft.**

I. INTRODUCTION

Today's automotive traction motors demand a very high torque as well as power density, plus a large overload capability. In addition, such motors also require a small size and low mass. These factors together bring about the desired vehicle performance [1]. Furthermore, the traction motors must also have a large speed range to operate at full capacity [2]. In order to achieve these requirements, high density as well as high frequency of current, plus a large number of magnets particularly for permanent magnet machines, need to be employed. As a result, electrical losses in the various components can be quite significant. Moreover, during operation the traction motors generate very severe levels of heat resulting from these losses. In order to minimize this level of overheating, a highly effective cooling and ventilating system has to be incorporated into the optimal design of such motors [3]. It can ensure sufficient heat removal from the motor inside. On top of this, a better cooling performance of rotor will result in higher power density, better field weakening capability and reduced costs.

There are several ways to cool the automotive traction motors. The forced air cooling, along with cooling fins integrated in the housing, is employed in the Tesla Roadster [4]. In such a motor, the internal and external air flows are improved to extract heat most effectively. The air cooling is a robust process, which is easily integrated, maintained and operated. However, for some applications, the power-to-dimension ratio of motor has to be greater, with a higher efficiency and lower noise level. The requisite outputs cannot be attained by the air cooling, the water cooling system is often applied. Using a housing water jacket is the most common water cooling approach. This is employed in the Toyota Prius [5], the Sonata [6], the Nissan Leaf [7] and the BMW i3 [8]. The main drawback with the housing water jacket cooling system is that the inner rotor is far away from the coolant. This leads to a poor heat dissipation condition within the rotor and causes a serious over-heating problem. In order to overcome this drawback, an extra rotor cooling system is then used in such later-developed vehicles as the Tesla S60 [9], where the coolant is introduced into the system via a coupling connected to a stationary inner tube and is driven back to the gap between the injection tube and the hollow shaft. In addition, hollow-shaft cooling scheme has been combined with housing cooling [10] and the end winding spray cooling [11, 12]. The much more detailed cooling approaches for automotive traction motors can be found in [13].

In cases where the coolant enters a hollow-shaft rotating about its axis, a secondary flow perpendicular to the direction of main flow is induced due to the tangential force. As a result, the convective heat transfer phenomenon of rotational flow are relatively different from that observed in a nonrotating flow. The rotational effects on the heat exchange have been investigated by different authors. For a fully laminar flow, a destabilizing effect has been convincingly demonstrated by reference [14], which observes that the flow characteristics cannot be maintained and the turbulent burst occurs. Consequently, the convective heat transfer rate between the cylinder inner wall and the airflow has a significant increase caused by this destabilizing effect [15]. However, in the context of fully turbulent flows, this destabilizing effect cannot be observed in a rotating pipe based on the findings in reference [16]. Furthermore, reference [17] points out that rotation has a stabilization effect in the axially rotating pipe flow. Pressure loss is considerably reduced at high rotating velocities when compared to a non-rotating flow. Moreover, reference [18] shows that the rotation of hollow-cylinder reduces the heat exchange rate if the flow is initially turbulent. However, these findings are pertinent to situations which have a high length-to-diameter ratio. They are invalid for such a hollow-shaft cooling system where a low length-to-diameter ratio is employed. Reference [19] concludes that at pipe entrance, the convective heat exchange on the pipe internal face increases with both rotational speed and axial air flow rate. However, at 840 rpm,

the heat exchange is mainly governed by rotational speed, with axial air flow velocity only slightly impacting this rate. In addition, reference [20] points out that both rotational speed (up to 4500 rpm) and axial flow rate can boost the heat exchange between the water and the heated hollow cylinder. However, in the literature hitherto, only low rotation speeds have been looked at. This means that there is still work to be done in relation to the effects of high rotational speeds on heat exchange. Moreover, all coolants up to now have been air / water-based. In reality, most coolants used in the automotive traction motors are oil-based.

This paper addresses the thermal performance of the oil-cooled shaft evaluated for use in the automotive traction motor, as identified in reference [21]. Various rotational speeds (up to 30,000 rpm) were investigated with a view to assessing the effects of high rotational speeds on heat exchange. On this basis, a detailed distribution of the electrical and mechanical losses in the shaft is set out in Section II. In Section III the thermal performance of this cooling method is evaluated using lumped parameter thermal network (LPTN) and computational fluid dynamics (CFD) approaches. Section IV describes the experimental mechanisms and measurement techniques. Section V offers a discussion of the impact parameters on this cooling performance.

II. STRUCTURE DESIGN AND POWER LOSSES CALCULATION

A. Test Rig Structure

Instead of using a whole machine, only a hollow-shaft made of EN43 carbon steel is employed to evaluate the thermal performance. A cross section view of experimental prototype is displayed in Fig. 1. This shaft is supported by two spindle ball bearings, where the bearings are adapted to the housing in order to suppress high-speed vibration. Then a uniform magnetic field perpendicular to the shaft axis is created by supplying Direct Current (DC) in the coils. As a consequence, when driven by an electric motor, iron loss is created in the magnetic shaft. At the same time, hydraulic oil* is forced through the shaft hole to cool the shaft. It is noted here that the hollow shaft would be fully filled with oil due to centrifugal forces caused by rotation. The properties of the hydraulic oil and the steel are shown in Table I and Table II, respectively. In addition, low friction rotary shaft seals are installed at ends of the shaft in order to prevent oil leakage. It is noted here that iron loss generated in the shaft is the main heat source of this rig. Moreover, the amount of iron loss is easy to control by adjusting the DC and the speed of shaft at test stage.

B. Power Losses

An accurate estimation of the heat loss and its distribution is a prerequisite of a proper thermal analysis. The major losses in the rig can be divided into following: electrical and mechanical types. The electrical losses are calculated by the time-stepping two-dimensional Finite Element Analysis (FEA) using JMAG, but windage loss is calculated by using analytical methods. In addition, the seal and flow friction losses are not taken into account here. It is because that these losses do not act as an internal heat source but are dissipated into the flow directly.
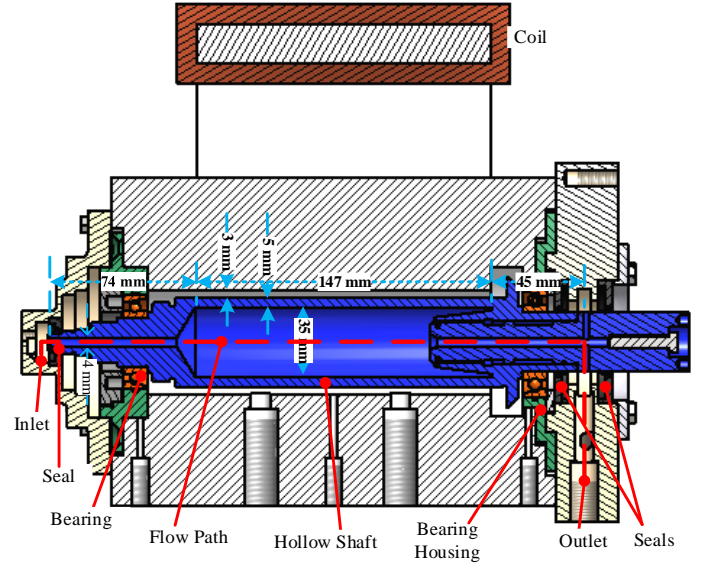
*Shell Tellus S2 M22

Fig. 1. Cross section view of the test rig.

TABLE I
HYDRAULIC OIL PROPERTIES AS PER TEMPERATURE T [℃].

Density, ρ [kg/m³]	$\rho = -0.60412T + 875.3$
Dynamic viscosity, μ [kg/(m·s)]	$\mu = 0.33928e^{-0.046826T}$
Specific heat , c_p [J/(kg·K)]	$c_p = 4.3533T + 1948$
Thermal conductivity k, [W/(m·K)]	$k = -7.2883e^{-5}\,T + 0.1351$

TABLE II
STEEL PROPERTIES AS PER TEMPERATURE T [℃].

Specific heat c_p, [J/(kg·K)]	$c_p = 0.6204T + 472.1$
Thermal conductivity k, [W/(m·K)]	$k = -0.03326T + 52$

a) Electrical Losses

Iron loss is the majority of losses generated in the shaft and depends on the strength of magnetic field as well as the rotating speeds. The iron loss P_{iron} in this solid shaft structure is calculated by integrating the current loss density over the volume of the region V using following equation:

$$P_{iron} = \int_V J \cdot E \qquad (1)$$

where J is the current density, E is the electrical field.

Iron loss density mainly comes from distortion of flux line on the shaft surface. Hence the calculation accuracy can be increased by taking into account the skin effect. In addition, the calculation time must be small enough to capture the frequency of eddy current development. As a result, the size of the shaft mesh is set at 1 mm with a 1.5 mm skin depth across all 5 divisions. As an example, the iron loss distribution at 5,000 rpm is shown in Fig. 2.
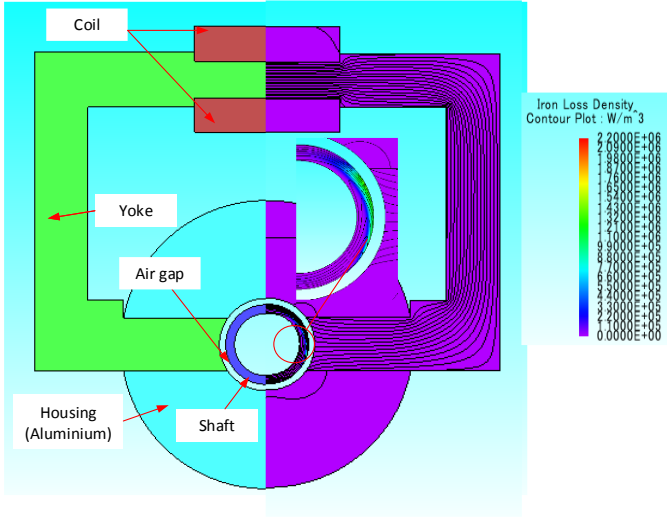
Fig. 2. Iron loss distribution in the rig.

b) Air Friction Loss

Air friction loss is generated by the tangential velocity from a rotating speed in the air gap. The value of this loss is dependent on rotating velocity of the shaft and this should not be negligible at high speeds. The following equation [22] is used to calculate this friction loss.

$$P_{F\_A} = kC_f\pi\rho\omega^3 r^4 l \tag{2}$$

where ρ is the density of air; k, l and r are the roughness coefficient, length and radius of the shaft respectively; ω is angular speed; C_f is the air friction coefficient, which depends upon the air gap geometry and shaft surface condition, can be expressed as (3) and (4). In order to better understand C_f, the Couette–Reynolds number Re_δ is introduced to describe the nature of tangential air flow. The definition of Re_δ is described as (5), which takes into account the effect of the enclosure by including the radial air-gap length.

$$C_f = 0.515\frac{(\delta/r)^{0.3}}{Re_\delta^{0.5}}, \quad 500 < Re_\delta < 10^4 \tag{3}$$

$$C_f = 0.0325\frac{(\delta/r)^{0.3}}{Re_\delta^{0.2}}, \quad Re_\delta > 10^4 \tag{4}$$

$$Re_\delta = \rho\omega r\delta/\mu \tag{5}$$

where μ is the air dynamic viscosity; δ is the radial air-gap length.

III. THERMAL MODELLING

A. The Lumped Parameter Thermal Network (LPTN) for Static State

In order to better highlight the dynamic effects due to the rotating speeds, the shaft is required to be stationary. However, iron loss cannot be generated when the shaft is at rest. On this basis, a simplified LPTN for these static states has been provided. For such static modelling, the heat transfer coefficient h between the shaft inner surface and the coolant is from an empirical correlation defined as (6) [23]. From the developed

LPTN model, the rise of the shaft temperatures is obtained in relation to these static conditions at various iron losses.

$$Nu = 3.66 + \frac{0.065 \times (D_h/L \times Re \cdot Pr)}{1 + 0.04 \times (D_h/L \times Re \cdot Pr)^{2/3}} \tag{6}$$

$$Nu = h \cdot D_h/\lambda \tag{7}$$

$$Re = \rho \cdot D_h \cdot V/\mu \tag{8}$$

$$Pr = \mu \cdot c_P/\lambda \tag{9}$$

where Nu, Re and Pr are the Nusselt, Reynolds and Prandtl numbers, respectively; D_h is the shaft hole hydraulic diameter, L is the length of the shaft; V is the inlet coolant flow rate; ρ, λ, μ and c_P are the density, thermal conductivity, dynamic viscosity and specific heat of the coolant .
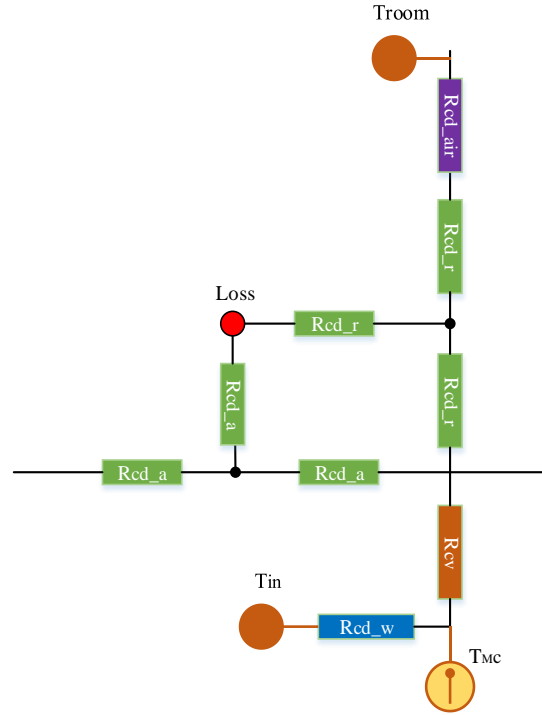

Fig. 3. One layer of developed TRN model.

To simplify the construction of the LTPN in relation to the rig at rest, only the shaft is modeled and radiation is not considered because of small area of emitting body. Iron losses, which are only heat source, are employed in the model. In the LPTN model, the shaft is divided into five layers, with three central layers representing the active section, plus two side layers representing the inlet and outlet sections. Fig. 3 shows the diagram of one layer LPTN model, where T-equivalent block method proposed in [24] is employed to calculate different kinds of thermal-conduction resistance. These resistances are displayed as green blocks R_{cd_a} and R_{cd_r}, which represent the axial and radial heat flows in the shaft respectively. The orange block Rcv, which is defined as (10), associates with heat exchange between the shaft and the flow. In addition, an equivalent thermal conductivity R_{cd_air}, -see

(11), is used to simulate the natural convection heat transfer across the air-gap to the housing, where the housing is set at room temperature. The thermal conductive resistance of the coolant is R_{cd_w}, visualized as a light blue block – defined in (12). Furthermore, the input temperature (T_{in}) of coolant is modelled as the output temperature of previous layer and this output temperature is measured by temperature meter (T_{MC}). Furthermore, the shaft's initial temperature is the same as that of the inlet coolant.

$$R_{cv} = \frac{1}{hA} \tag{10}$$

$$R_{cd\_air} = \frac{L}{\lambda A} \tag{11}$$

$$R_{cd\_w} = \frac{1}{mc} \tag{12}$$

In (10)-(12), A is the cross-sectional area of heat flow path; L is the length of heat transfer path; m and c are the mass and the specific heat capacity of flow, respectively.

B. Computational Fluid Dynamics for Dynamic Modelling

a) Model definition and Mesh

Fig. 4 shows a three-dimensional (3-D) CFD model in the STAR-CCM+, where is developed to evaluate the thermal performance of the hollow-shaft cooling system. In this diagram, the solid region of model is represented by grey domain, whereas the blue areas stand for fluid regions. The properties of fluid and solid regions in this model are from Table I and Table II. Polyhedral elements are employed to create a 3-D mesh with a size set at 2 mm. Polyhedral meshing is chosen due to its relative ease of creation and increased efficiency owing to its use of fewer cells than tetrahedral meshes. In addition, conformal meshes are used to encompass separate solid and fluid elements without interrupting the continuity of the mesh between these contacting parts. Moreover, prismatic cell layers are added next to the wall boundaries to capture velocity and thermal boundary layers. The mesh size is set to be 2 mm and 10 prime layers are used to generate orthogonal prismatic cells next to wall surfaces with ratio of 1.4 for layer stretching. This 3-D mesh not only provides a higher near-wall mesh density, but also allows high-aspect-ratio cells to be used, thus offering a better and more effective solution in the heat transfer and swirling flow situations.
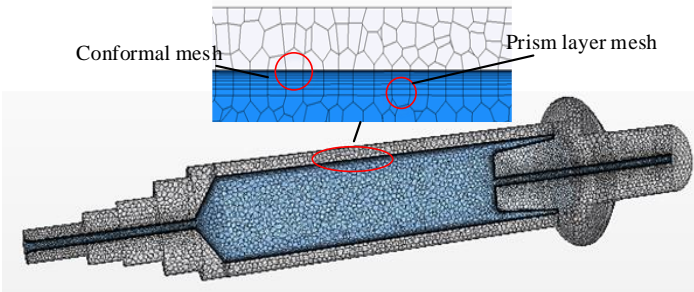

Fig. 4. 3D Mesh in CFD.

b) Governing Equations

In this CFD model, the Reynolds-Averaged Navier-Stokes (RANS) equations are used to solve and analyse the mechanics of fluids. To obtain the RANS equations (13-14), the variable in the instantaneous Navier-Stokes equations is decomposed into its averaged value U_i and fluctuating quantities u_i'.

$$\frac{\partial U_i}{\partial x_i} = 0 \tag{13}$$

$$\rho \frac{\partial}{\partial x_j}\left(U_i U_j\right) = -\frac{\partial P}{\partial x_i} + \frac{\partial}{\partial x_j}\left(2\mu S_{ij} - \rho \overline{u_i' u_j'}\right) \tag{14}$$

where P is the pressure force; S_{ij} is the strain-rate tensor and can be expressed as

$$S_{ij} = \frac{1}{2}\left(\frac{\partial U_i}{\partial x_j} + \frac{\partial U_j}{\partial x_i}\right) \tag{15}$$

The quantity $\tau_{turb} = -\rho \overline{u_i' u_j'}$ is known as the Reynolds stress tensor and defined as following.

$$\tau_{turb} = -\rho \overline{u_i' u_j'} = -\rho \begin{pmatrix} \overline{u'u'} & \overline{u'v'} & \overline{u'w'} \\ \overline{u'v'} & \overline{v'v'} & \overline{v'w'} \\ \overline{u'w'} & \overline{v'w'} & \overline{w'w'} \end{pmatrix} \tag{16}$$

By decomposing the instantaneous properties into time-averaged and fluctuating components, additional unknown quantities are introduced. The same number of closure equations are necessary to solve these unknowns. In the following section, several approaches (turbulence models) are described in order to solve the RANS equations.

The energy change of fluid element is equivalent to the heat into this element plus the work done by surface forces. However, the energy change due to mechanical force is neglectable. This energy only important for the flow with high viscosity and velocity gradient. On this basis, the energy conservation equation can be expressed as:

$$\rho C_p U_j \frac{\partial T}{\partial x_j} = \lambda \frac{\partial^2 T}{\partial x_j \partial x_j} \tag{17}$$

The heat equation needs to be calculated for both the solid region and the fluid domain. For solid heat conduction, the velocity components are set to zero

c) Turbulent Models

The turbulence models provide closure relations for the RANS equations and govern the Reynolds stress tensor. The basic approach is to employ eddy viscosity models based on Boussinesq assumption to model the Reynolds stresses tensor as a function of mean flow quantities. In this assumption, the Reynolds stresses is linked to the mean strain rate of deformation through eddy viscosity μ_t, and defined as (18).

$$-\rho \overline{u_i u_j} = 2\mu_t S_{ij} - \frac{2}{3}\rho k \delta_{ij} \tag{18}$$

where k is the turbulence kinetic energy; δ_{ij} is the Kronecker delta which is a function of two variations, $\delta_{ij} = 1$, if $i = j$ and $\delta_{ij} = 0$ otherwise. Two different eddy viscosity models are selected to calculate the turbulent eddy-viscosity in this case: Realizable K-Epsilon with two-layer approach [25] and Shear-Stress Transport (SST) K-Omega model. In addition, Reynolds Stress Transport (RST) models, referred to as second moment closures, are also employed in his study. The key benefit of RST models is that the assumption in eddy-viscosity models is avoided and the components of the specific Reynolds stress tensor in (16) are directly calculated. Moreover, directional effects of the Reynolds stresses as well as complex interactions in turbulent flows are also accounted for in these models.

d) Wall Modelling

In fluid mechanics, the near-wall region of boundary layer can be split into three layers. For RANS turbulence models, the wall treatment provides boundary conditions to solvers for turbulence and imposes values of the transported turbulence quantities on centroids of near-wall cells. To apply the law of the wall, the flow velocity u^+ and wall distance y^+ in wall velocity profiles are expressed in dimensionless form as:

$$u^+ = \frac{u}{\sqrt{\tau_w/\rho}} \quad (19)$$

$$y^+ = \frac{\rho y \sqrt{\tau_w/\rho}}{\mu} \quad (20)$$

where y is normal distance from the wall, τ_w is the wall shear stress.

In this study, an All y+ Wall Treatment model [26] is applied for the profile of the mean flow quantities in the wall boundary layers. All y+ Wall Treatment is a hybrid approach that seeks to represent the behaviors of both the Low y+ Wall Treatment and High y+ Wall Treatment in the limit of very fine or very coarse meshes. It is also developed with the desirable feature of providing reasonable results for intermediate meshes where the cell centroid falls within the buffer layer. The final value for these turbulence quantities are calculated by the blending approach [26]. Consequently, a high resolution mesh is created at the wall boundary layer with wall cell y+ ≤ 0.2 in order to obtain accurate predictions in relation to the turbulence parameters.

e) Moving Reference Frame and Boundary Conditions

The modelling of rotation in CFD is crucial due to the strong effects of rotation on the flow and pressure drop in the shaft. Consequently, a moving reference frame (MRF) is created to generate a constant rotating force in order to mimic the rotation. A MRF is to freeze the moving bodies in a specific position and observe the instantaneous flow field in that position. As a result, the MRF is an efficient approach to modelling certain systems involving constant rigid body motion using the steady state solver.

The losses that have been discussed in Section II are applied into the shaft as the heat source with a uniform distribution. The heat transfer coefficient of the shaft external surface is modelled as a smooth annular gap known as the Taylor-Couette flow. The Nusselt number for air gap is expressed as (21) based on the Taylor number [27]. The air gap convection heat transfer coefficient h is evaluated by applying (7).

$$Nu = \begin{pmatrix} 2, Ta < 1700 \\ 0.128\, Ta^{0.367}, 1700 < Ta < 10^4, \\ 0.409\, Ta^{0.241}, 10^4 < Ta < 10^7 \end{pmatrix} \quad (21)$$

On this basis, all heat is dissipated to the coolant through forced convection from the shaft inner wall to the coolant on one side and from the shaft outer surface to the air gap on the other.

IV. EXPERIMENT SETUP

A. Setup

The flow diagram of the experimental setup is shown in Fig. 5. The cooling loop consists of a circulation system, where oil is pumped into the hollow-shaft after passing through a heat exchanger and is then recirculated from a container. The oil temperature that flows through the test rig is controlled by absorbing or dissipating heat from the water in the heat exchanger. The water temperature that enters the heat exchanger can be set at a constant value by a water heater. The oil flow rate can vary and is measured using a flow meter. In addition, an electric motor attached to the shaft with a pulley allows for the shaft to rotate at up to 30,000 rpm.
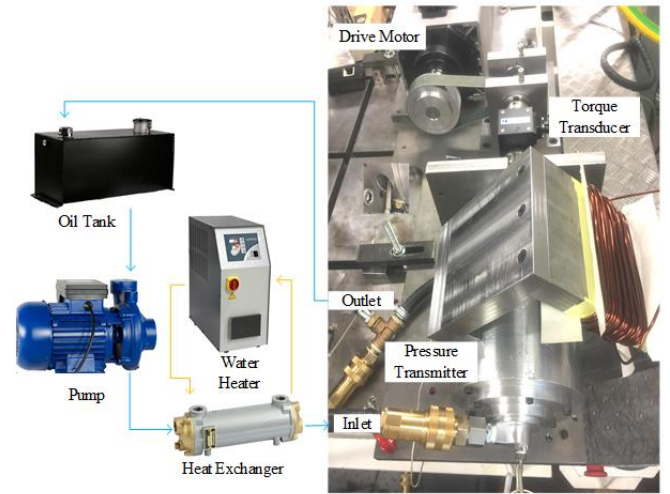

Fig. 5. Experimental test rig (blue arrow for the oil loop, orange arrow for the water loop).

B. Loss Measurement

The input power of the test rig can be defined (22) by measuring the torque and angular speed. As shown in Fig. 5, a torque transducer is placed between the shaft and the electrical motor to measure the torque τ. The shaft angular speed ω_s can be obtained by (23), where ω_m is the electric motor speed and η is the belt acceleration ratio (3.26 for all experiments).

$$P_{input} = \omega_s * \tau \quad (22)$$

$$\omega_s = \omega_m * \eta \qquad (23)$$

Based on the law of conservation of energy, the input power is all transferred to the electrical loss $P_{elec-loss}$ and mechanical loss $P_{mech-loss}$ as defined in (24)

$$P_{input} = P_{elec-loss} + P_{mech-loss} \qquad (24)$$

$P_{elec-loss}$ are mainly from iron loss in the shaft and the pole core. However, the core iron loss is not considered due to small amount of current. In order to measure these losses separately, two different steps were taken by spinning the shaft with direct current off and on, respectively. When DC is off, the input power P_{off} is only transferred into $P_{mech-loss}$, which includes the air friction, bearing friction, seal friction and flow dynamic losses. Then switch on the DC, the input power P_{on} is from not only $P_{mech-loss}$ but also iron losses $P_{elec-loss}$. Therefore, the net loss ($P_{on} - P_{off}$) is the iron losses caused by the shaft.

C. Temperature Measurement

Two non-contact infrared temperature sensors, which are mounted in the middle of the housing, are used to measure temperatures of the shaft surface. Consideration is given to the colour of the shaft surface, which is painted black in order to increase the surface emissivity. The calibration of infrared temperature sensors was measured against a reference OMEGA Surface Mount 4 wire Pt100 element temperature sensor with an accuracy of ± 0.07 ℃. The test setup was mounted with thermocouples and inserted into a Carbolite oven at a range of 20 to 100 ℃ with 0.5 ℃ hysteresis. After measurement, the infrared thermometer offset was at 0.71 ℃. As for the coolant, two four-wire Pt100 sensors are mounted in two ends of the housings to measure the inlet and outlet coolant temperatures. Furthermore, the air gap, the coil and the pole temperature are measured using K type thermocouples and taken as indication in thermal model. The locations of infrared sensor and thermocouples are shown in Fig. 6.
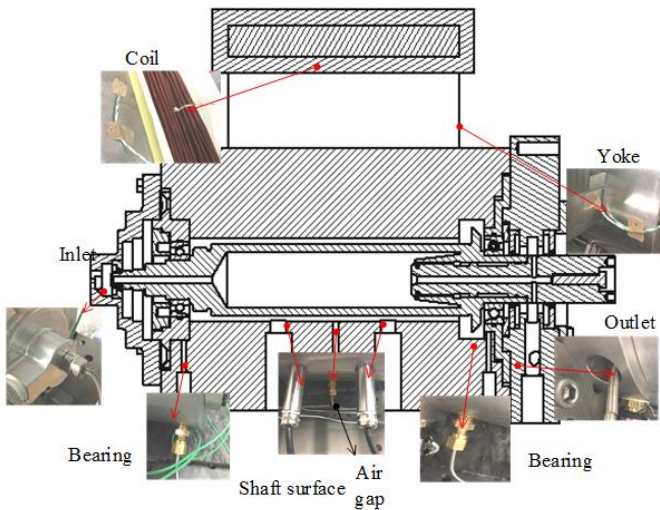

Fig. 6. Temperature sensor locations.

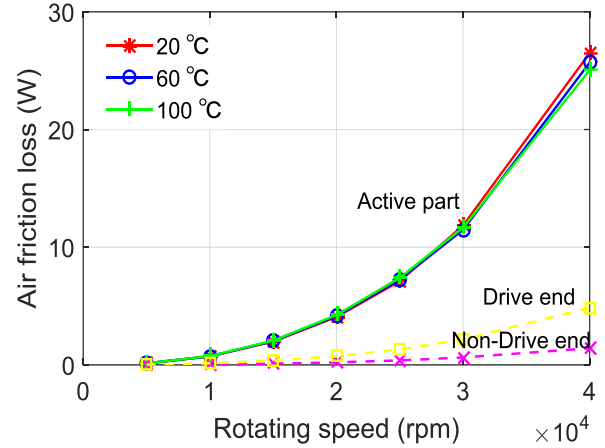## V. RESULTS AND DISCUSSIONS

A. Power Losses

Fig. 7. Friction losses on the shaft surface and end face.

Friction loss of the shaft surface at various rotating speeds and air temperature are shown in Fig. 7. The roughness coefficient is taken as 1.0 for smooth surfaces. The plots on the graph show that air friction losses are proportional to rotation speed. But the rise in air temperature has the effect of slightly decreasing friction loss. The predominant reason for the slight decrease of air friction loss with increasing temperature is because an increase in air temperature leads to a decrease in the air density. Though the viscosity of air increases with temperature, the effect of the air density decrease outweighs the contrary effect of the air viscosity rise. This leads to a decrease in the cohesive forces of the air molecules and causes a lower shear stress during the rotation of the shaft, resulting in a decrease of air friction loss.
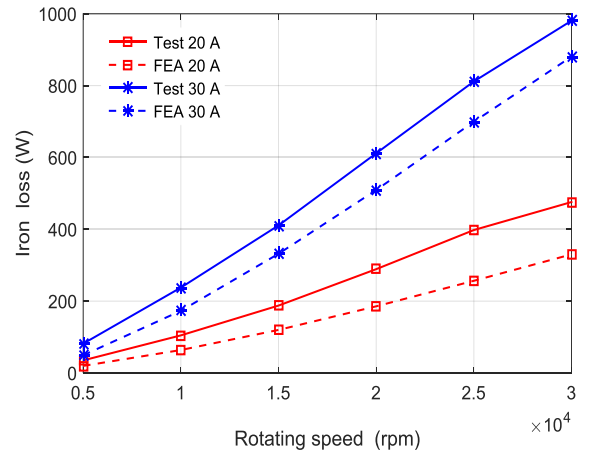

Fig. 8. Iron loss curves versus the rotational speed and the input current.

A comparison of the results obtained between experiments and FEA-predicted variations of iron losses is shown in Fig. 8. It can be concluded that the value of loss increases with the rise in the rotational speed and the input current. To explain this, two phenomena can be addressed: Firstly, the distortion frequency of magnetic field in the shaft is enhanced due to the rise of rotating speed. Secondly, the rise of the input current boosts the uniform magnetic flux density. As a consequence, the current density in the shaft rises due to these effects. The 2-

D FEA simulation underestimates the iron loss. This is because only the active part of shaft was taken into account for the iron loss calculation. In reality, the leakage flux would pass through the ends of shaft, causing extra losses. In addition, the effect of manufacturing on the constructed shaft is not considered in the FEA simulation. Cutting and welding during the manufacturing process induce mechanical stresses in steels, leading to the deterioration of the material magnetic properties [28]. Consequently, more iron loss would be generated in the experiment than in the FEA prediction due to the effects of mechanical manufacturing.

B. Shaft Temperature Rise at the Various Rotational Speeds

The comparison of the shaft temperature rise at various rotational speeds between experimental and numerical results is shown in Table III, where iron losses were manually adjusted to approximately 410 W at 22 °C inlet temperature.

TABLE III
COMPARISON OF THE SHAFT TEMPERATURE RISE.

Speed (rpm)	T rise (℃)			
	Experiment	CFD (Realizable k- ε)	CFD (SST k- ω)	CFD (RST)
0	101.8 (LPTN)	-	-	-
5000	65.3	34.8	44.4	52.1
10000	42.1	26.4	32.9	36.7
15000	36.0	23.6	28.6	30.4
20000	30.7	23.3	27.0	28.4
25000	28.1	22.6	25.4	26.4
30000	26.9	21.8	24.9	25.2

It is noted here that the shaft temperature decreases with the rotating speed in experimental testing and CFD simulations. When the shaft is rotating, the coolant becomes destabilised due to the tangential forces caused by rotation, which makes the flow more turbulent. The level of destabilization flow increases with the rise in rotational speed. The critical speed of this study is around 2000 rpm when the critical rotational Reynolds number $Re_r = \rho \cdot D_h \cdot V_r / \mu$ (V_r is the tangential velocity) of that the laminar flow starts to transition is around 2300 [29]. Specifically, under conditions where the iron losses remain at 410 W the following results can be observed: at 5000 rpm above the stationary level, the shaft rotation can significantly reduce temperature of the shaft surface. To explain this effect, three phenomena can be identified: Firstly, the rotation of the shaft has a destabilizing effect on the coolant. As a result, the heat transfer between the shaft wall and the coolant particles is boosted. Secondly, the coolant in the shaft hole center tends to move radially to the shaft inner wall due the centrifugal effect caused by rotation. This phenomenon promotes heat exchange between the cold and warm fluid. Thirdly, the tangential velocity enhances the value of air gap convection heat transfer coefficient. However, when the shaft rotating velocity rises, the temperature of the shaft reduces slightly and tends to be constant between 25,000 and 30,000 rpm. It seems that the effect of high rotational speeds on heat exchange weakens due to the flow is becoming stable.

It is also noticed that two eddy viscosity based models display a higher discrepancy than RST model. This is due to the fact that the Reynolds stress tensors in these eddy viscosity approaches are modelled as a linear function of the mean flow quantities. In addition, turbulent eddy viscosity is assumed to be isotropic based on Boussinesq approximation. In comparison, RST models are usually more accurate in complex flow configurations because the Reynolds stress-tensor components are directly solved from governing transport equations. Moreover, the effects of turbulence anisotropy and swirl rotation are naturally accounted for. However, the second-moment closure RST model carries significant computational overhead as five additional equations must be solved.
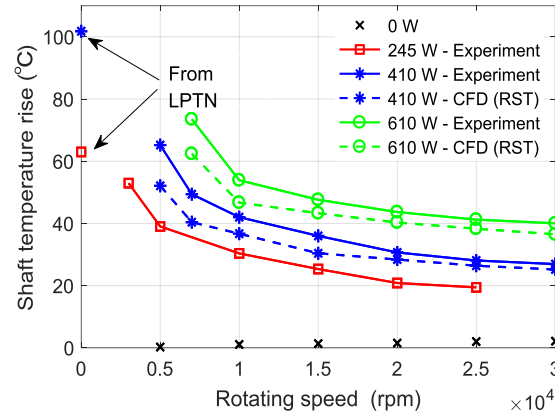
C. Shaft Temperature Rise at Various Iron Loss

Fig. 9 Shaft temperature rises at various rotating speeds for different iron loss.

The rise of shaft temperature resulting in different iron losses at 22 °C inlet temperature is displayed in Fig. 9. When iron loss is 0, the increase in the shaft surface temperature stems from air friction loss. At 30,000 rpm, the rise of shaft temperature is less than 2 ℃. Then iron losses have been adjusted to 245 W, 410 W and 610 W respectively. The difference in losses at various speeds are within ± 2 % of each other. The flow rate of the coolant is similar in all experiments (about 4.2 L/min). As was anticipated, for a given cooling configuration the temperatures of the shaft increase as iron losses also rise. The decreases in the shaft temperature show a similar trend along the rotational speed axis with different iron losses.

D. Shaft Temperature Rise at Various Flow Rates

A number of flow rates have been carried on in relation to various rotating speeds with the temperature of the coolant at 22 ˚C. Fig. 10 shows that the shaft temperature decreases with the inlet coolant velocity when the shaft is at non-rotating. However, when the rotational speed of the shaft is at 5000 rpm or 10,000 rpm, the shaft temperature remains quite constant at various inlet velocities. The influence of the inlet flow rate on internal heat exchange is then negligible. In another words, heat transfer between the shaft and the coolant is only governed by rotational speed. The laminar flows are totally destabilized due to the effects of rotation.
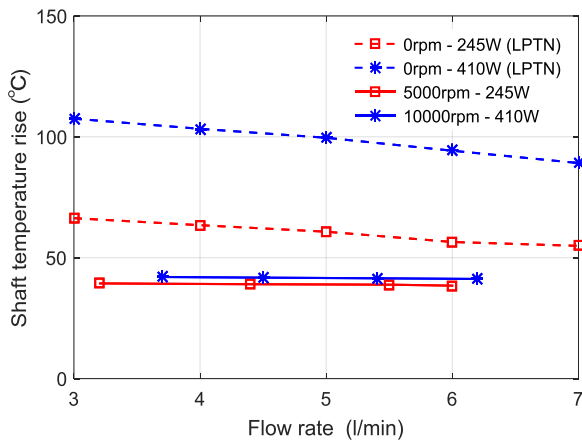
Fig. 10 Shaft temperature rise at various flow rates.

VI. Conclusion

In this paper, the thermal performance of an oil cooled hollow-shaft as applied to a high speed automotive traction motor is addressed. RANS turbulence modelling based on CFD is proposed to estimate the relation between rotation effects and convective heat transfer. By comparing with data from the experimental prototype, it is noticed that the second class of RST models have the potential to predict rotating flow more accurately than the first class of eddy viscosity models. However, the computations of the second order scheme demands highly time-consuming.

More importantly, as compared to steady state case, it is concluded that the shaft temperature drops sharply in both simulation and testing. This is explained that a destabilizing effect is created by the shaft rotation. Consequently, the heat transfer is thus enhanced by rotation. However, when the rotational velocity increases, the flow becomes to be stable. And the effects of rotation on heat exchanges are almost non-existent when the angular velocity reaches 30,000 rpm. Moreover, the amount of loss and the inlet flow rate have a very limited impact on performance of this cooling system. Finally, this paper also provides a practical solution for the machine designers to overheating issue of automotive traction motors.

VII. References

[1] J. D. Widmer, R. Martin, and B. C. Mecrow, "Optimization of an 80-kW Segmental Rotor Switched Reluctance Machine for Automotive Traction," *IEEE Transactions on Industry Applications,* vol. 51, no. 4, pp. 2990-2999, 2015.

[2] J. H. J. Potgieter, F. J. Márquez-Fernández, A. G. Fraser, and M. D. McCulloch, "Performance evaluation of a high speed segmented rotor axial flux switched reluctance traction motor," in *2016 XXII International Conference on Electrical Machines (ICEM)*, pp. 531-537.

[3] A. M. El-Refaie *et al.*, "Advanced High-Power-Density Interior Permanent Magnet Motor for Traction Applications," *IEEE Transactions on Industry Applications,* vol. 50, no. 5, pp. 3235-3248, 2014.

[4] *[Online]. Available: https://web.archive.org/web/20100705130833/http://www.teslamotors.com:80/roadster/technology/motor . 2010.*

[5] T. A. Burress *et al.*, "Evaluation of the 2010 Toyota Prius Hybrid Synergy Drive System," Oak Ridge Nat. Lab., Oak Ridge, TN, USA, Rep. ORNL/TM-2010/253, 2011, Available: http://www.osti.gov/scitech/servlets/purl/1007833.

[6] T. Burress, "Benchmarking competitive technologies," presented at the 2012 U.S. Dept. Energy Hydrogen Fuel Cells Program Veh. Technol. Program Annu. Merit Rev. Peer Eval. Meeting, U.S. Department of Energy, MD, USA, 2012.

[7] T. Burress, "Benchmarking State-of-the-Art Technologies," presented at the 2013 U.S. Dept. Energy Hydrogen Fuel Cells Program Veh. Technol. Program Annu. Merit Rev. Peer Eval. Meeting, U.S. Department of Energy, MD, USA, 2013., Available: http://energy.gov/sites/prod/files/2014/03/f13/ape006_burress_2013_o.pdf.

[8] T. Burress, "Electrical Performance, Reliability Analysis, and Characterization," presented at the 2017 U.S. Dept. Vehicle Technologies Office Annual Merit Review, U.S. Department of Energy, MD, USA, 2017.

[9] M. Popescu, D. A. Staton, A. Boglietti, A. Cavagnino, D. Hawkins, and J. Goss, "Modern Heat Extraction Systems for Power Traction Machines-A Review," *IEEE Transactions on Industry Applications,* vol. 52, no. 3, pp. 2167-2175, 2016.

[10] K.-H. Lee, H.-R. Cha, and Y.-B. Kim, "Development of an interior permanent magnet motor through rotor cooling for electric vehicles," *Applied Thermal Engineering,* vol. 95, pp. 348-356, 2016/02/25/ 2016.

[11] S. Sano, T. Yashiro, K. Takizawa, and T. Mizutani, "Development of New Motor for Compact-Class Hybrid Vehicles," *World Electric Vehicle Journal,* vol. 8, no. 2, pp. 443-449, 2016.

[12] K. S. Bennion, "Electric Motor Thermal Management Research: Annual Progress Report," United States2017-10-19 2017, Available: http://www.osti.gov/scitech/servlets/purl/1404876.

[13] Y. Gai *et al.*, "Cooling of Automotive Traction Motors: Schemes, Examples, and Computation Methods," *IEEE Transactions on Industrial Electronics,* vol. 66, no. 3, pp. 1681-1692, 2019.

[14] K. Kikuyama, M. Murakami, K. Nishibori, and K. Maeda, "Flow in an Axially Rotating Pipe : A calculation of flow in the saturated region," *Bulletin of JSME,* vol. 26, no. 214, pp. 506-513, 1983.

[15] G. Reich, B. Weigand, and H. Beer, "Fluid flow and heat transfer in an axially rotating pipe-II. Effect of rotation on laminar pipe flow," *Heat and Mass Transfer,* vol. 32, no. 3, pp. 563-574, 1989.

[16] M. Murakami and K. Kikuyama, "Turbulent Flow in Axially Rotating Pipes," *Journal of Fluids Engineering,* vol. 102, no. 97, pp. 97-103, 1980.

[17] A.White, "Flow of A Fluid in an Axially Rotating Pipe," *Journal Mechanical Engineering Science* vol. 6, no. 1, 1964.

[18] G. Reich and H. Beer, "Fluid flow and heat transfer in an axially rotating pipe—I. Effect of rotation on turbulent pipe flow," *International Journal of Heat and Mass Transfer,* vol. 32, no. 3, pp. 551-562, 1989.

[19] S. Seghir-Ouali, D. Saury, S. Harmand, O. Phillipart, and D. Laloy, "Convective heat transfer inside a rotating cylinder with an axial air flow," (in English), *International Journal of Thermal Sciences,* vol. 45, no. 12, pp. 1166-1178, 2006.

[20] Y. Gai *et al.*, "On the Measurement and Modeling of the Heat Transfer Coefficient of a Hollow-Shaft Rotary Cooling System for a Traction Motor," *IEEE Transactions on Industry Applications,* vol. 54, no. 6, pp. 5978-5987, 2018.

[21] M. Kimiabeigi *et al.*, "High-Performance Low-Cost Electric Motor for Electric Vehicles Using Ferrite Magnets," *IEEE Transactions on Industrial Electronics,* vol. 63, no. 1, pp. 113-122, 2016.

[22] Y. Gai, Y. C. Chong, H. Adam, J. Goss, and M. Popescu, "Power Losses and Thermal Analysis of a Hollow-Shaft Rotor Cooling System," in *2019 22nd International Conference on Electrical Machines and Systems (ICEMS)*, 2019, pp. 1-6.

[23] D. A. Staton and A. Cavagnino, "Convection Heat Transfer and Flow Calculations Suitable for Electric Machines Thermal Models," *IEEE Transactions on Industrial Electronics,* vol. 55, no. 10, pp. 3509-3516, 2008.

[24] J. Nerg, M. Rilla, and J. Pyrhonen, "Thermal Analysis of Radial-Flux Electrical Machines With a High Power Density," *IEEE Transactions on Industrial Electronics,* vol. 55, no. 10, pp. 3543-3554, 2008.

[25] W. Rodi, "Experience with two-layer models combining the k-epsilon model with a one-equation model near the wall," in *29th Aerospace Sciences Meeting* (Aerospace Sciences Meetings: American Institute of Aeronautics and Astronautics, 1991.

[26] "User Guide STAR-CCM + Version 10.06," CD-adapco, Melville, NY, USA, 2015.

[27]   D. A. Howey, P. R. N. Childs, and A. S. Holmes, "Air-Gap Convection in Rotating Electrical Machines," *IEEE Transactions on Industrial Electronics,* vol. 59, no. 3, pp. 1367-1375, 2012.

[28]   K. Bourchas *et al.*, "Influence of cutting and welding on magnetic properties of electrical steels," in *2016 XXII International Conference on Electrical Machines (ICEM)*, 2016, pp. 1815-1821.

[29]   K. T. Trinh, "On The Critical Reynolds Number For Transition From Laminar To Turbulent Flow," Institute of Food Nutrition and Human Health, Massey University, New Zealand,2011, Available: https://arxiv.org/ftp/arxiv/papers/1007/1007.0810.pdf.